Scripta Materialia 193 (2021) 71–76

Contents lists available at ScienceDirect

Scripta Materialia

journal homepage: www.elsevier.com/locate/scriptamat

Multiscale characterization of the 3D network structure of metal carbides in a Ni superalloy by synchrotron X-ray microtomography and ptychography

Zhiguo Zhang[a,b], Jia Chuan Khong[c], Billy Koe[b,d], Shifeng Luo[b], Shi Huang[b], Ling Qin[b], Silvia Cipiccia[d], Darren Batey[d], Andrew J. Bodey[d], Christoph Rau[d], Yu Lung Chiu[e], Zhu Zhang[f], Jean-Christophe Gebelin[f], Nick Green[e], Jiawei Mi[b,*]

[a] Institute of Advanced Wear & Corrosion Resistant and Functional Materials, Jinan University, Guangzhou, 510632, China
[b] Department of Engineering, University of Hull, East Yorkshire HU6 7RX, United Kingdom
[c] Department of Medical Physics & Biomedical Engineering, University College London, London WC1E 6BT, United Kingdom
[d] Diamond Light Source, Harwell Science and Innovation Campus, Didcot OX11 0DE, United Kingdom
[e] High Temperature Research Centre, School of Metallurgy and Materials, University of Birmingham, B15 2TT, United Kingdom
[f] Doncasters Group Technical Centre, George Baylis Rd, Droitwich WR9 9RB, United Kingdom

ARTICLE INFO

Article history:
Received 1 September 2020
Accepted 16 October 2020
Available online 1 November 2020

Keywords:
Synchrotron X-ray microtomography
Ptychography
Metal carbides
IN713LC Ni superalloy

ABSTRACT

Synchrotron X-ray microtomography and ptychography were used to characterize the 3D network structure, morphology and distribution of metal carbides in an as-cast IN713LC Ni superalloy. MC typed carbides were found to distribute mainly on the grain boundary between the matrix γ and γ' phase. The differences in solidification cooling rate had a minor influence on the volume fraction of the MC type carbides, but significantly affected the carbide size, distribution and network morphology. Depending on the local composition of the remaining liquid phase and geometric constraints, the carbides can form either spherical or strip or network morphologies. The research demonstrated clearly the advantage and technical potential of using the two complementary tomography techniques synergistically to characterize non-destructively complex multiple-phase structures in three dimensional space with a spatial resolution of ~30 nm.

Nickel based superalloys have been extensively used for making high-temperature structural components in aircraft and land turbine engines, rocket engines, nuclear power and chemical processing plants [1-4]. These superalloys are designed to have a unique microstructure where the ordered intermetallic $\gamma'(Ni_3Al)$ precipitates distribute coherently within a continuous γ(Ni) matrix. Such microstructural features provide substantial ordered and coherent interfaces to inhibit dislocation motion at higher temperature, delivering superior high-temperature strength and creep resistance [5-7]. For cast Ni superalloys, the γ-phase is the primary phase formed during solidification while the γ'-phase mainly nucleates and grows within the interdendritic region at the final stage of solidification.

Metal carbide is another important microstructure constituent in polycrystalline Ni-based superalloys due to its excellent high-temperature stability. The carbide is originally designed to improve high-temperature strength through strengthening the grain boundary and preventing grain boundary sliding [8-9]. However, carbide can also cause crack initiation and propagation during plastic deformation [10-12]. The morphology and spatial distribution of the carbides in cast Ni superalloys are mainly formed through the solidification process and therefore have an important influence on the solidified microstructures and the mechanical properties [13-14]. Although considerable researches have been carried out to investigate the nucleation, growth and morphology evolution of the carbides in Ni-based superalloys under different solidification conditions [15-17], until now, the nucleation and growth dynamics of metal carbides, especially the true 3-dimensional (3D) network structure and morphology of metal carbides formed in different solidification conditions have not been fully understood.

Carbides in the as-cast Ni-based superalloys are usually MC (*M*=Ti, Nb, Ta and V) type compounds with NaCl face-centred-cubic structure. They form in the liquid melt due to strong segrega-

* Corresponding author.
E-mail address: J.Mi@hull.ac.uk (J. Mi).

https://doi.org/10.1016/j.scriptamat.2020.10.032

Table 1
Chemical compositions of the IN713LC Ni superalloy.

C	Cr	Al	Mo	Nb	Ti	Co	Fe
0.05	12	5.9	4.68	2.31	0.77	0.41	0.15
Ni	**Cu**	**Ta**	**Mn**	**Si**	**B**	**P**	**S**
Bal.	<0.05	<0.05	<0.05	<0.05	<0.012	<0.007	<0.007

tion of C when its concentration is above 0.05% [18]. Depending on the solidification conditions, the carbides can form different spatial structure and morphologies. They could be octahedral or irregular blocky or script-typed morphologies in a 2D sectional view when they grew in slow-cooling, near-equilibrium solidification conditions [19-21]. In contrast, in a rapid cooling condition, such as in laser surface melting, the morphology of MC carbides can vary and form a peculiar structure, i.e. radially branched flower-like colonies [22-23]. These growth morphologies are proposed to be related to the typical faceted growth mechanism where the lateral growth from existing steps or ledges originating from the closed packed {111} planes, twins and screw dislocations on the growing crystal surfaces [15]. Until now, the carbide morphologies were mostly studied using 2D imaging methods, only giving limited information on their true 3D characteristics, and their spatial interconnections and correlations with other phases. Nonetheless, recent studies have shown that 3D phase differentiation and visualization of carbides in Ni-based superalloys are possible by focused ion beam (FIB) assisted Electron Back-Scattered Diffraction (3D-EBSD) [24] or atom probe tomography (APT) [25]. However, these techniques are normally for characterising local region of small volume in the diameter range of a few tens or a few hundreds of nanometres, not suitable for the measurement of volume fractions and the true 3D spatial distribution of the carbides.

In this paper, we were focusing on multiscale characterizing the metal carbides in an as-cast polycrystalline IN713LC Ni superalloy. Synchrotron X-ray microtomography and ptychography methods were used synergistically to study the 3D network structures, distribution and the correlations of the carbides with other solidified phases, providing quantitative and true 3D information for understanding the mechanism of phase formation and transformation during the solidification of this alloy.

The chemical composition of the IN713LC Ni superalloy used in this study is shown in Table 1. This alloy was melted and cast using a specially-designed mould to form wedge-shaped samples as shown in Fig. 1a. This shaped sample resulted in different cooling rates at different locations of the sample. The cooling rates along the central symmetrical line of the wedge was calculated based on the temperature measurement. Plate samples with typical cooling rates of 0.27 K/s (in the thicker end) and 1.12 K/s (in the thinner end) were cut from the as-cast wedge samples for microstructure characterization.

The 2D microstructure observation of the carbides was carried out by using a Zeiss Evo60 Environmental scanning electron microscopy (SEM). The samples were ground and then polished. A chemical solution (100 ml C_2H_5OH, 100 ml HCl and 5 g $CuCl_2$) was used to deeply etch the sample surface to expose the carbides.

Synchrotron X-ray microtomography experiments were conducted at Beamline I13–2 of Diamond Light Source (DLS), UK [26-28]. For this experiment, the square bars cut from the wedge sample were further ground into circular needle shape (Insert in Fig. 1a). The schematic experimental setup diagram and parameters used in this study can be found in the supplements and in Table 2. Tomography reconstruction was performed using the computing cluster at I13 of DLS based on a filtered back projection algorithm [29].

The ptychographic X-ray computed tomography (PXCT) experiment was carried out at the I13–1 Coherence Branchline of DLS, UK [26]. Ptychography is a scanning coherent small angle scattering technique with a lensless geometry, therefore aberration free and theoretically diffraction limited [30]. The diagram of experimental setup of PXCT can be found in the supplements and the details are described in Fig. 1c of Ref [31]. The Excalibur detector was used to record the diffraction patterns in the far field [32]. The sample geometry for PXCT experiment is shown in the insert of Fig 1a. The detailed experimental procedure can be found in the supplements. Ptychographic reconstruction on each scan projection was performed with PtyREX Code [33] while the 3D reconstruction was conducted with the Savu processing pipeline software [34], using the ASTRA Recon GPU implementation of filtered-back projection algorithm [35]. The segmentation, visualization and analyses for both synchrotron X-ray tomographic and 3D ptychographic datasets were conducted by using Avizo 9.4 software (FEI VSG, France).

Fig. 1b shows the obtained secondary electron SEM micrograph for the deep-etched sample with a cooling rate of 0.27 K/s. The primary dendrite is marked by the white dotted lines, showing a typical FCC structural growth morphology where the dendritic arms grew preferably along the low index crystal directions, e. g., ⟨100⟩ [36]. The carbides distributed either within the interval of secondary arms or in the interdendritic region. Several typical carbide morphologies in the Ni-based superalloy can be distinguished for both samples with 0.27 K/s and 1.12 K/s cooling rates. Fig 1c-e show the irregular blocky, strip and symmetric cross-petal-like morphologies of the carbides, respectively. All these carbide morphologies suggest that the carbide branches grew along {111} face of the cubic cores, as marked by yellow dotted rectangles in the figures. The octahedron with {111} face is the equilibrium MC carbide morphology due to the minimum carbide-liquid interface energy [20]. The cubic cores are the 2D projections of the octahedral MC carbides. The contrast variation surrounding the cubic cores suggests there might be chemical composition gradients and thus the formed carbides are composites, as reported in other studies for IN713LC Ni-base superalloy [37-39]. Fig. 1f presents a typical complex script-like carbide network morphology, which also consists of octahedral cores and plate carbide branches.

Fig. 2a, b and the companying video #1 show the 3D network structure of the carbides in a relatively large volume for the two samples with different cooling rates. It is clear that the carbide network distributed along the edge of the secondary dendrite arms in 3D space and within the interdendritic region, consistent with the previous 2D observation. However, in contrast to the coarser secondary dendrite arm for the sample with a low cooling rate of 0.27 K/s (Fig. 2a), the interval of the secondary dendrite arms became smaller for the sample of a higher cooling rate of 1.12 K/s (Fig. 2b), which led to the smaller local volume for the carbide network. Moreover, it was found that the spherical (blocky type in 2D view) and irregular rod (strip type in 2D view) carbides were predominant in the sample with a high cooling rate in spite of sometime formation of some small carbide networks (Fig. 2d). On the other hand, the spherical and rod carbides interconnected each other and formed compact and complex carbide networks in the sample with a low cooling rate of 0.27 K/s (Fig. 2c). Such feature is often observed as script-typed carbides in a 2D projection view. The complex carbide network is due to the further growth of the spherical and rod carbides and coalescence between each other [20].

For quantitative statistical analysis of the 3D characteristics of the carbides, a high-level combination module with watershed, distance transform and numerical reconstruction algorithms in the Avizo software was firstly used to separate individual carbides in 3D space. The separated individual carbides were then grouped in three categories: spherical, rod and network carbides based on their 3D shape characteristics and further confirmed by visual in-

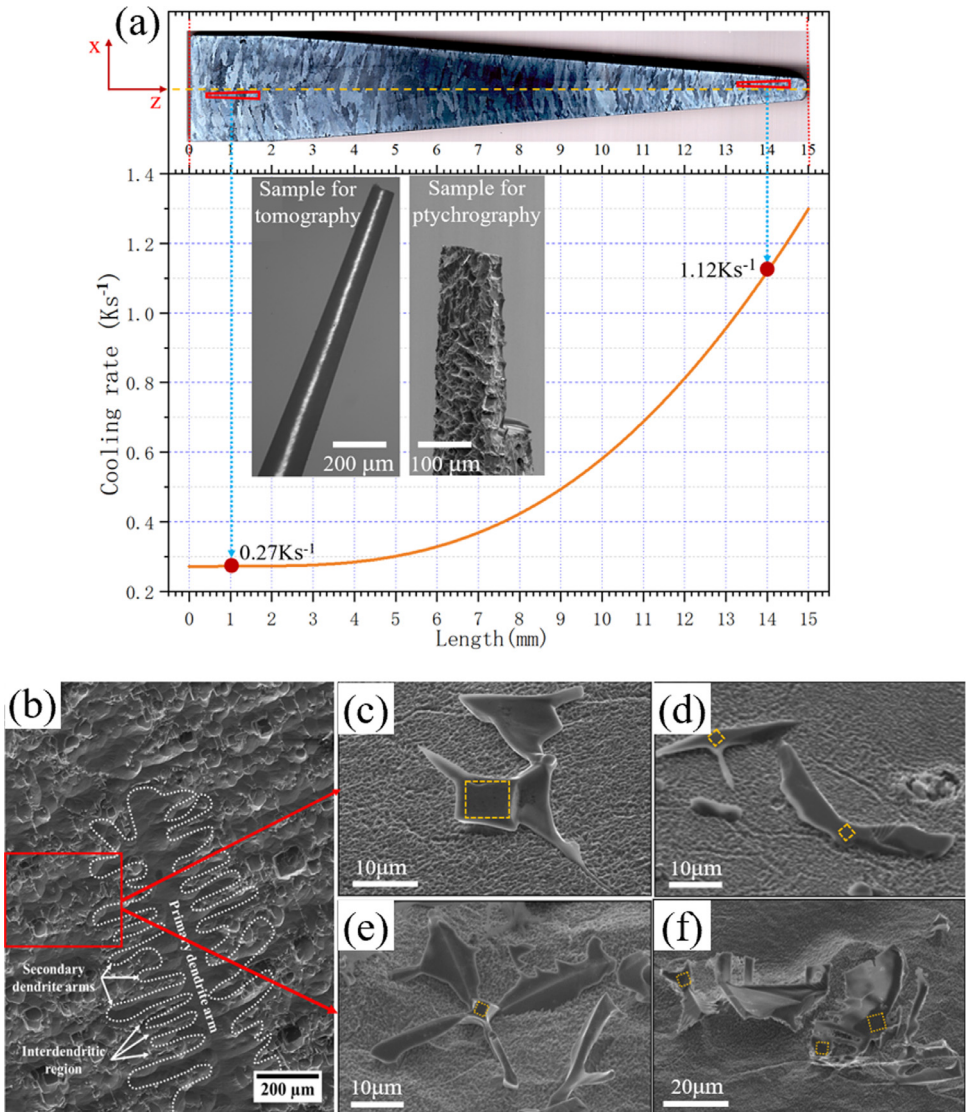

Fig. 1. The as-cast wedge-shaped Ni sample and samples machined into different geometries for tomography and ptychography measurement, as well as the deeply-etched morphologies. (a) the as-cast wedge-shaped sample with different cooling rates along its central symmetry line; (b) The deeply-etched morphology for the sample with a 0.27 K/s cooling rate; (c) The typical irregular blocky carbide; (d) the strip carbide; (e) the cross-petal-like carbide and (f) the script-like carbide.

Table 2
Parameters used for the tomography and ptychography acquisition at the I13 beamline, DLS.

Parameters	Tomography in I13–2	Ptychrography in I13–1
X-ray beam energy	18.5 KeV	20 KeV
Scintillator	GGG: Eu	–
Detector	pco.edge 5.5 (PCO AG, Germany)	Excalibur
Effective magnification	20 ×	–
Effective pixel size	0.33 μm	Detector pixel size: 50 um Reconstructed pixel size 30 nm
Field of view of projection	2560 × 2160 pixels	2400 × 2400 pixels
Exposure time	1.9 s/projection	0.1 s/scanning step
Sample-to-scintillator distance	10 mm	14.6 m
No. of projections for 3D tomography	2000	400
Rotation degree range (°)	180	180

spection. Quantification analysis results for the different categories are given in Table 3. The total volume fraction of carbides in the sample of 0.27 K/s cooling rate is 1.04%, quite similar to the value (1.18%) in the sample of 1.12 K/s cooling rate. This result indicates that the variation of cooling rates in the present study had minor influence on the obtained carbide volume fraction. The average particle size for the spherical carbides was ~13 μm^3 in both the samples with different cooling rates. Such results were consistent with previous reports which revealed that the cooling rate in a wide range from 0.10 to 50 K/s had little influence on either the solidification sequence or degree of micro-segregation [39-40]. This is mainly due to the facts that the formed carbides are MC-typed, for which the stronger C formation elements i. e. Ti and Nb can easily react with C. However, the average particle sizes for the rod

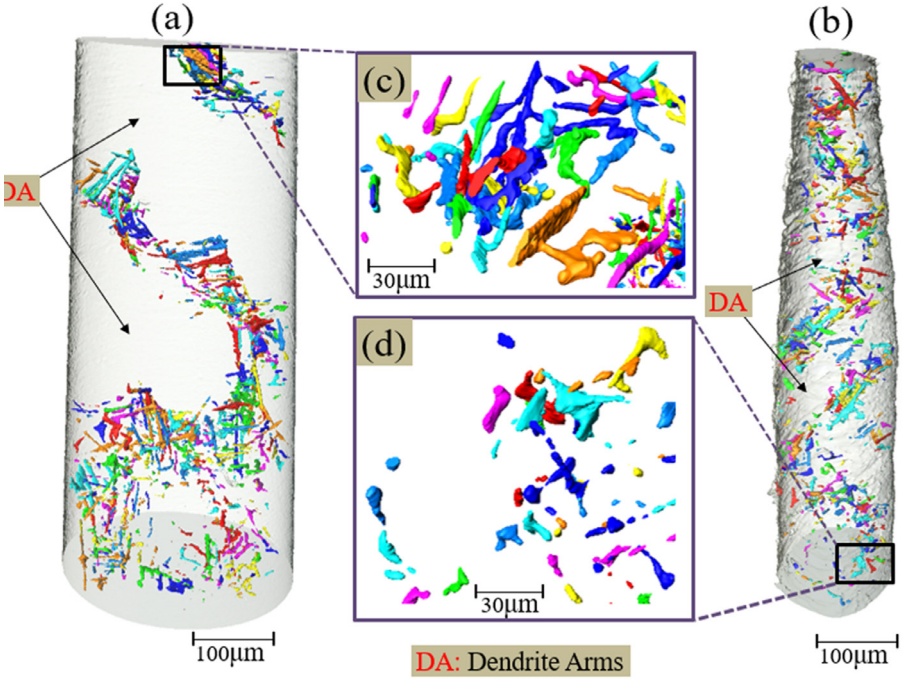

Table 3. The statistic results for different category carbides.

Cooling rate	Carbides		Spherical Carbides			Rod Carbides			Network Carbides		
K/s	Volume (μm^3)	Volume Fraction (%)	Volume (μm^3)	Number	Average Size (μm^3)	Volume (μm^3)	Number	Average Size (μm^3)	Volume (μm^3)	Number	Average Size (μm^3)
0.27	64658	1.04	8345	663	13	39592	426	93	16720	51	328
1.12	35690	1.18	6355	463	14	24726	281	88	4609	16	288

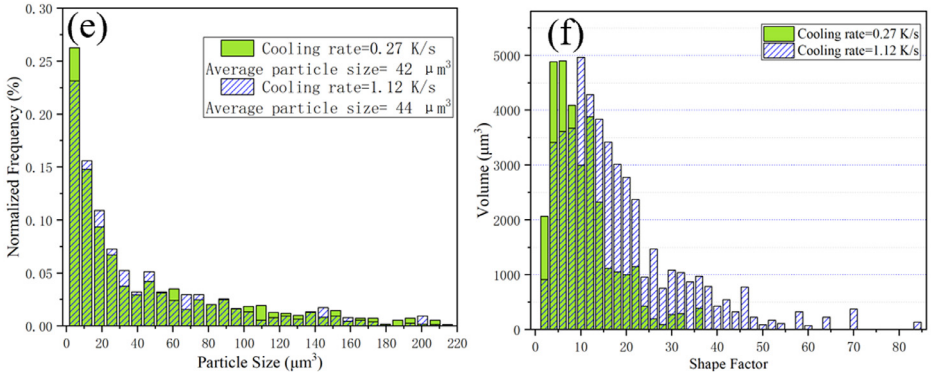

Fig. 2. The 3D morphologies, distribution and network of the carbides. (a) and (b) are the 3D morphology and network of the carbides in the samples with cooling rate of 0.27 K/s and 1.12 K/s, respectively; (c) and (d) are the enlarged local carbide morphology for (a) and (b); (e) and (f) are the particle size distribution and the shape factor distribution for the spherical and rod carbides.

carbides in the 0.27 K/s sample were 97 μm^3, increased by 10% when compared to that (88 μm^3) obtained in the 1.12 K/s sample, confirming the further growth and coalescence of the carbides due to having sufficient diffusion time in the low cooling rate sample. In particular the average size of the network carbides changed from 288 to 328 μm^3, increased by 14% when the cooling rate reduced from 1.12 to 0.27 K/s.

Fig. 2e and f shows the statistic distribution characteristics of the spherical and rod carbides. Due to the tiny amounts of the network carbides and the significant difference on volume between the network carbides and the other two categorized carbides, the distribution of network carbides was not included in the figures. Fig. 2e indicates that the reduction of cooling rate led to a slight increase in the average particle size (44 vs. 42 μm^3). Fig. 3f presents the shape factor distribution for the spherical and rod carbides. The shape factor is defined as $= \frac{S^3}{36\pi V^2}$, where S is the measured total surface area for an individual carbide and V corresponds to its individual volume. This morphology parameter represents the shape characteristics of the individual carbides, and 1 represents a perfect sphere. The comparison of the shape fac-

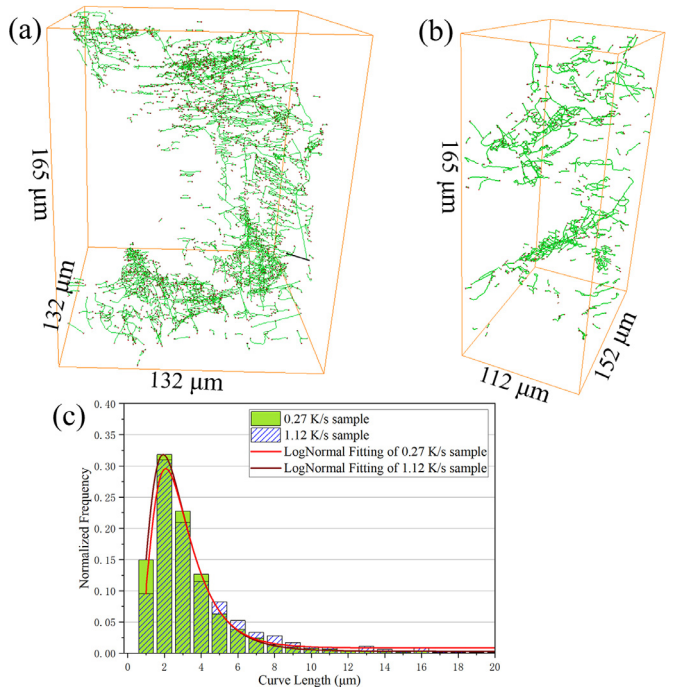

Fig. 3. Skeleton of the carbides in:(a) sample with 0.27 K/s cooling rate and (b) sample with 1.12 K/s cooling rate; (c) the curve length distribution for the carbide branches.

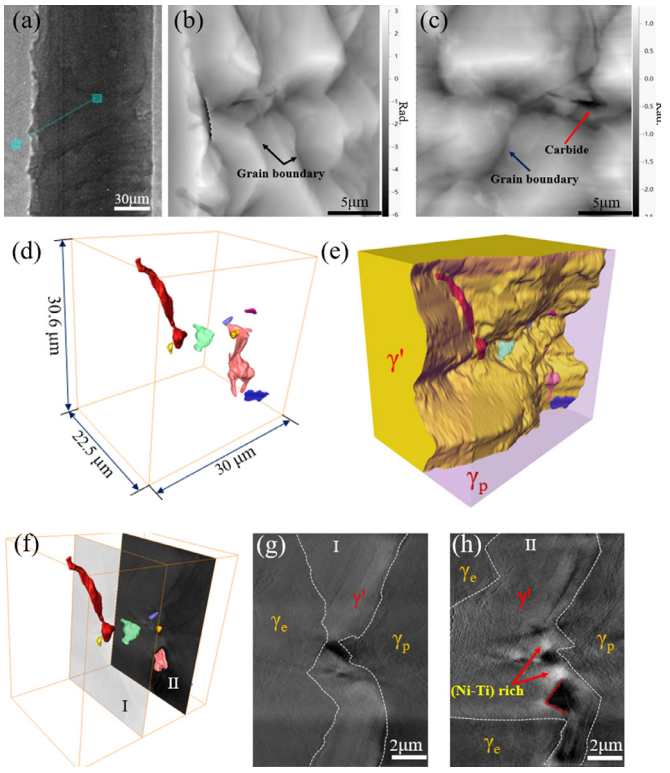

Fig. 4. X-ray ptychography image and tomography for the carbides in the sample with a cooling rate of 1.12 K/s. (a) a transmission projection; (b) and (c) are the retrieved 2D projections at −83.5° and 45°, respectively; (d) 3D morphologies for the carbides with a higher resolution of 30 nm; (e) the correlations of carbides, γ and γ' phases in 3D space; (f) indicates the extract slice positions for (g) and (h); (g) shows the spherical carbide and its correlation with other phases; (h) is the strip carbide and its correlation with other phases.

tor distribution for the samples with different cooling rates reveals that the individual carbides continuous growth transitions from the spherical morphology to rod morphology when reducing the cooling rate.

The skeletonization function in Avizo software was used to peel off parts of the typical 3D carbide networks down to a skeleton of 1 voxel in thickness. The 3D characteristics of the carbide branches can be visualized (Fig. 3a and b), illustrating the growth paths of the carbide branches during solidification [41]. The 3D characteristics of the carbide skeleton were then quantified by counting statistically the curve length between each node. The statistical curve length distributions are shown in Fig. 3c. The statistic results followed Lognormal distribution for both cases in different cooling rates. The peak position in the 0.27 K/s sample slightly shifts into longer length when compared to that in the 1.12 K/s sample, indicating that the slow cooling rate produced more proportionally branches of a greater curve length.

Fig. 4 shows the synchrotron X-ray ptychography image and tomographic morphologies for the 1.12 K/s sample. This imaging method provides a higher spatial resolution of 30 nm and also the correlation of different phases. Fig 4a is a transmission projection perpendicular to the deep-etched surface, showing the interconnected carbide network in the region. The retrieved 2D projections at −83.5° and 45° (Fig. 4b and c) revealed the stereo-morphologies of the interfaces for γ' phases in the alloy. The reconstructed 3D tomography, however, presents the true 3D shapes of the irregular spherical and rod (plate in 2D view) carbides, as shown in Fig. 4d and the accompanying video #2. All these carbides located at the grain boundaries between the matrix γ phase and γ' phase (Fig. 4e, the γ phases are rendered as semi-transparent). Fig. 4g and h show the typical 2D slices containing carbides extracted from the 3D tomographic dataset, revealing that the dominant growth directions of carbide branches were mainly determined by the local composition of the remaining liquid phase and geometric constraints. The positions of the slices are indicated in Fig. 4f. Fig. 4g and the accompanying video 2 also show the detailed correlations of the primary γ_p, eutectic γ_e, carbides and γ' phase in 2D view. In Fig. 4g, the γ' phase demonstrated a relative homogenous constitution while the carbide presents a short blocky (spherical carbides in 3D) morphology embedded on the boundary of primary γ_p, eutectic γ_e and γ' phases. The solidification path of this morphology was L→γ; L→γ + MC + (γ +γ'), as proposed by other researchers [39-41]. Fig. 4g shows that parts of the core of the strip carbide seemed to be within the γ' phase. However, detailed observation of the carbides in most other slices indicated that the strip carbide cores were located at the boundary of γ phase. The different contrast within the γ' phase suggested the γ' phase was not homogeneous in composition, which might be due to the further segregation of Nb, Ti elements in this case. Taking into account the chemical composition of the IN713LC superalloy, Nb and Ti elements prefer to react first with C and also can segregate into γ' phase during the solidification while Cr, Mo and Al can segregate into both γ phase and γ' phase [37]. Therefore, the composition of γ' phase on the vicinity of the MC carbide is likely a Nb-Ti rich phase, as indicated in Fig. 4h. This result is similar to and consistent with that reported for IN713LC superalloy [39]. Hence, the solidification path in such case is proposed as L→γ; L→γ + MC + (γ +γ') + (Nb-Ti rich phase).

In summary, synchrotron X-ray microtomography revealed and quantified the 3D characteristics of the spherical, strip and network structure of the metal carbides in an as-cast IN713LC Ni superalloy. Synchrotron X-ray ptychography revealed that the individual MC carbides were distributed on the grain boundary between the matrix γ and γ' phases. The dominant growth directions of carbide branches were mainly determined by the local composition of the remaining liquid phase and geometric constraints.

Declaration of Competing Interest

The authors declare that they have no known competing financial interests or personal relationships that could have appeared to influence the work reported in this paper.

Acknowledgments

The authors wish to make the following acknowledgements: Project Funding & Financial Support: the Royal Society Industry Fellowship (for J. Mi in 2012–2016), and the Chinese Scholarship Council Scholarship (No. 201806785038 for Z. Zhang's visiting fellowship at University of Hull in 2019–2020); The relevant synchrotron X-ray beamtime awarded by the Diamond Light Source (MT9974, MT13488 and MG22525); access to the University of Hull supercomputer, Viper and the assistance by the support team (Mr Chris Collins in particular) for data analysis and visualization.

Supplementary materials

Supplementary material associated with this article can be found, in the online version, at doi:10.1016/j.scriptamat.2020.10.032.

References

[1] R.R. Unocic, G.B. Viswanathan, P.M. Sarosi, S. Karthikeyan, J. Li, M.J. Mills, Mater. Sci. Eng. A 483–484 (2008) 25–32.
[2] Pollock Tresa, Tin Sammy, J. Propuls. Power 22 (2) (2006) 361–374.
[3] Stoichko Antonov, Wei Chen, Jiajie Huo, Qiang Feng, Dieter Isheim, N David, Seidman, eugene sun and sammy tin, Metallur. Mater. Trans. A 49 (2018) 2340–2351.
[4] N.D. S.ouza, H.B. Dong, Script. Mater. 56 (2007) 41–44.
[5] R. Lawitzki, S. Hassan, L. Karge, J. Wagner, D. Wang, J. von Kobylinski, C. Krempaszky, M. Hofmann, R. Gilles, G. Schmitz, Acta Mater. 163 (2019) 28–39.
[6] R. Cozar, A. Pineau, Met. Trans. 4 (1973) 47–59.
[7] Haibo Long, Shengcheng Mao, Yinong Liu, Ze Zhang, Xiaodong Han, J. Alloy. Comp. 743 (2018) 203–220.
[8] L.Z. He, Q. Zheng, X.F. Sun, H.R. Guan, Z.Q. Hu, A.K. Tieu, C. Lu, H.T. Zhu, Mater. Sci. Eng. A 397 (2005) 297–304.
[9] C.-.N. Wei, H.-.Y. Bor, L. Chang, Mater. Sci. Eng. A 527 (2010) 3741–3747.
[10] A. Pineau, S.D. Antolovich, Eng. Fail. Anal. 16 (2009) 2668–2697.
[11] J. Jiang, J. Yang, T. Zhang, J. Zou, Y. Wang, F.P.E. Dunne, T.B. Britton, Acta Mater. 117 (2016) 333–344.
[12] Paraskevas Kontis, David M. Collins, Angus J.Wilkinson, Roger C. Reed, Dierk Raabe, Baptiste Gault, Script. Mater. 147 (2018) 59–63.
[13] Seung-Yong Lee, Byung-Kyu Kim, Sang-Hyeok Lee, Dong-Ik Kim, Jae-Hyeok Shim, Woo-Sang Jung, Jin-Yoo Suh, J. Alloy. Comp. 813 (2020) 152222.
[14] B. Tang, L. Jiang, R. Hu, Q. Li, Mater. Char. 78 (2013) 144–150.
[15] H.M. Wang, L.C. Yu, X.X. Li, P. Jiang, Sci. Techno. Adv. Mater. 2 (2001) 173–176.
[16] H. Yu Z, L. Liu, X.B. Zhao, China Foundry 7 (4) (2010) 352–356.
[17] H. Yu Z, L. Liu, B. Zhao X, et al., China Foundry 7 (3) (2010) 217–223.
[18] H. Matysiak, M. Zagorska, J. Andersson, Materials (Basel) 6 (2013) 5016–5037.
[19] Jinfeng Nie, Yuying Wu, Pengting Li, Hui Li, Xiangfa Liu, Cryst. Eng. Comm. 14 (2012) 2213–2221.
[20] Zhang Weiguo, Liu Lin, Fu Hengzhi, China Foundry 9 (1) (2011) 11–14.
[21] Zhu-huan Y.U., Lin Liu and Jun Z.H.A.N.G., Trans. Nonferrous Met. Soc. China 24(2):339–345.
[22] Yen-Ling Kuo, Koji Kakehi, Metals (Basel) 7 (2017) 367–372.
[23] V. Divya, R. Muñoz-Moreno, O. Messé, J. Barnard, S. Baker, T. Illston, H. Stone, Mater. Char. 114 (2016) 62–74.
[24] M.A. Charpagnea, A.T. Polonsky, M.P. Echlin, S. Jacomet, J. deJaegerd, M. DeGraef, N. Bozzolo, T.M. Pollock, Script. Mater. 186 (2020) 109–113.
[25] Paraskevas Kontis, David M. Collins, Angus J.Wilkinson, Roger C. Reed, Dierk Raabe, Baptiste Gault, Script. Mater. 147 (2018) 59–63.
[26] C. Rau, U. Wagner, Z. Pešić, A. De Fanis, Phys. Status Solidi. A 208 (2011) 2522–2525.
[27] Z. Pešić, A. De Fanis, U. Wagner, C. Rau, J. Phys.: Conf. Series 425 (2013) 182003.
[28] C. Rau, U. Wagner, Z. Pešić, A. De Fanis, Physica Status Solidi 208 (2011) 2522–2525.
[29] M. Basham, J. Filik, M.T. Wharmby, P.C. Chang, B. El Kassaby, M. Gerring, J. Aishima, K. Levik, B.C. Pulford, I. Sikharulidze, J. Syn. Rad. 22 (2015) 853–858.
[30] J.M. Rodenburg, A.C. Hurst, A.G. Cullis, B.R. Dobson, F. Pfeiffer, O. Bunk, C. David, K. Jefimovs, I. Johnson, Phys. Rev. Lett. 98 (2006) 034801.
[31] Simone Sala, Darren J. Batey, Anupama Prakash, Sharif Ahmed, Christoph Rau, Pierre Thibault, Opt. Express 27 (2019) 533–541.
[32] S.J. Williams, D. Batey, S. Cipiccia, C. Angelsen, R. Crook, et al., in: Nuclear Science Symposium and Medical Imaging Conference (NSS/MIC), Atlanta, GA, 2017, pp. 1–3.
[33] D.J. Batey, Ptychographic Imaging of Mixed States PhD thesis, University of Sheffield, 2014.
[34] Robert C. Atwood, Andrew J. Bodey, Stephen W.T. Price, Mark Basham, Michael Drakopoulos, Phil. Trans. R. Soc. A. 373 (2015) 20140398.
[35] W. van Aarle, W.J. Palenstijn, J. Cant, E. Janssens, F. Bleichrodt, A. Dabravolski, J. De Beenhouwer, K. Joost Batenburg, J. Sijbers, Opt. Express 24 (22) (2016) 25129–25147.
[36] Chubin Yang, Lin Liu, Xinbao Zhao, Yafeng Li, Jun Zhang, Hengzhi Fu, Prog. Nat. Sci.: Mater. Inter. 22 (5) (2012) 407–413.
[37] N.D. S.ouza, M. Lekstrom, H.B. Dong, Mater. Sci. Eng. A 490 (2008) 258–265.
[38] Simona Zlá, Bedřich Smetana, Monika Žaludová, Jana Dobrovská, Vlastimil Vodárek, Kateřina Konečná, Vlastimil Matějka, Hana Francová, J. Therm. Anal. Calor. 110 (1) (2012) 211–219.
[39] N.D. S.ouza, H.B. Dong, M.G. Ardakani, B.A. Shollock, Script. Mater. 53 (2005) 729–733.
[40] T. Fredriksson, H. Antonsson, Metal. Mater. Trans. B 36 (2005) 85–96.
[41] Y. Zhao, W. Du, B. Koe, T. Connolley, S. Irvine, P.K. Allan, C.M. Schlepütz, W. Zhang, D.G.Eskin F.Wang, J. Mi, Script. Mater. 146 (2018) 321–326.